Sensors and Materials, Vol. 37, No. 6 (2025) 2589–2605
MYU Tokyo

S & M 4076

Applicability of the Geospatial Segment Anything Model for Reservoir Extraction Using KOMPSAT-3/3A Satellite Imagery

Namhoon Kim,[1] Suhong Yoo,[2] Hanna Lee,[3] Sumin Park,[4] and Gihong Kim[5*]

[1]Department of Civil Engineering and Environmental Sciences, Korea Military Academy,
574 Hwarang-ro, Nowon-gu, Seoul 01805, Republic of Korea
[2]Department of Drone and GIS Engineering, Namseoul University,
91 Daehak-ro, Seobuk-gu, Cheonan-si 31020, Republic of Korea
[3]Institute for Smart Infrastructure, Gangneung-Wonju National University,
7 Jukheon-gil, Gangneung-si 25457, Republic of Korea
[4]National Satellite Operation and Application Center, Korea Aerospace Research Institute,
Daejeon, Republic of Korea
[5]Department of Civil Engineering, Gangneung-Wonju National University,
7 Jukheon-gil, Gangneung-si 25457, Republic of Korea

(Received January 10, 2025; accepted April 23, 2025)

Keywords: remote sensing, deep learning, Segment Anything Model, image segmentation, water body extraction, reservoir monitoring, KOMPSAT-3/3A

Accurate reservoir area data are essential for effective water resource management, yet traditional field surveys often face labor and logistical challenges. In this study, we evaluated the Geospatial Segment Anything Model (GeoSAM) in conjunction with high-resolution KOMPSAT-3/3A satellite imagery for reservoir delineation in the Korean Peninsula. Our experiments demonstrate that GeoSAM consistently achieves high accuracies (85.95–97.10%), surpassing the conventional normalized difference water index-based extraction method, which averaged 93.74%. Moreover, GeoSAM maintains robust performance under challenging conditions—such as frozen reservoirs, shadowed areas, and cloudy environments—by incorporating additional point prompts. These findings underscore the potential of GeoSAM to advance remote sensing applications in water resource management, particularly for small- and medium-sized urban areas.

1. Introduction

1.1 Background

The accurate extraction of reservoir areas is essential for effective water resource management, as it is important for quantifying available water resources, facilitating hydrological modeling, and supporting infrastructure planning for citizens. This information is vital for estimating the reservoir capacity and enabling the development of sustainable water allocation policies. Moreover, it enhances climate change resilience by monitoring shifts in

[*]Corresponding author: e-mail: ghkim@gwnu.ac.kr
https://doi.org/10.18494/SAM5539

ISSN 0914-4935
https://myukk.org/

water bodies, contributing to biodiversity conservation efforts, and aiding in flood risk assessment. Reservoir area data are crucial for managing water quality, guiding land-use planning decisions, and ensuring equitable allocation of water resources, all of which collectively contribute to the development of comprehensive and sustainable water resource management strategies.

In contemporary water resource management, the application of remote sensing technologies to reservoir extraction represents a paradigm shift in the acquisition and analysis of critical hydrological data. Remote sensing, which encompasses a spectrum of technologies such as satellite imagery and aerial sensing platforms, has emerged as an invaluable tool for systematically and efficiently characterizing reservoirs. This methodological evolution is particularly more crucial than traditional field surveys, which are often labor-intensive, time-consuming, and constrained by logistical challenges.

A salient feature of remote sensing in the context of reservoir extraction is its capability to provide extensive coverage over large geographic areas. This capability transcends the limitations of on-site investigations and facilitates a comprehensive overview of reservoirs and their surrounding environments. The enhanced effectiveness inherent in remote sensing methodologies is underscored by the substantial reduction in costs and time associated with data acquisition, which is paramount in academic research and practical reservoir management. Numerous studies have delineated large reservoirs.(1–4) Broadly, the utilization of moderate resolution imaging spectroradiometer (MODIS) images characterized by low spatial resolution is primarily directed towards observing expansive lakes or reservoirs. Concurrently, active engagement has been generated in leveraging high-resolution Earth observation satellites, notably Landsat-8.

Moreover, remote sensing technologies' high spatial resolution capabilities contribute to the detailed delineation of reservoir boundaries, the identification of infrastructure, and the characterization of shoreline alterations. This granular-level analysis is pivotal for precision in reservoir extraction and enables a comprehensive assessment of the physical attributes of reservoirs. Water body extraction primarily relies on Sentinel(5–7) and Landsat(8–11) satellite images. High-resolution satellite imagery has also been employed for water body extraction.(12–14)

In numerous studies, diverse methodologies have been employed to precisely extract water areas encompassing lakes and reservoirs. The spectrum of approaches ranges from conventional methods, such as watershed area classification using the normalized difference water index (NDWI), to enhanced techniques, including those using the modified normalized difference water index (MNDWI). The efficacy of NDWI, a seminal water system extraction index introduced by Gao,(15) has been substantiated. Additionally, MNDWI, an index initially proposed by Xu,(16) was modified by substituting the near-infrared band with the middle-infrared band. This adaptation optimizes MNDWI for built-up areas, which is considered for its effectiveness in minimizing land noise. Guo *et al.*(17) introduced a weighted NDWI for enhancing the mapping accuracy of water bodies using Landsat imagery. Rokni *et al.*(18) employed various indicators, including NDWI, MNDWI, normalized difference moisture index, water ratio index, normalized difference vegetation index, and automated water extraction index (AWEI), to extract water body areas. The results revealed the superiority of NDWI over other indicators, and the study incorporated principal components of multitemporal NDWI (NDWI-PCs) to detect changes in surface water over time.

Accurate water body extraction through indicators, such as NDWI, crucially depends on precise threshold determination. Typically, thresholds are set to zero or determined using the Otsu algorithm;[17,19] however, inherent limitations exist in achieving precise threshold determination using these methods.[20] Various methods have been explored to address these issues. Ji *et al.*[21] ascertained the optimal threshold by examining NDWI variations across different combinations of infrared bands and water/nonwater ratios. They concluded that the optimal results can be achieved using a short-wave infrared band ranging from 1.2 to 1.8 μm. However, the threshold determination process requires a flexible approach. Considering the potential variation in the optimal NDWI threshold across different regions, using a universal threshold such as zero may result in diminished precision in water body extraction.[22,23] In addition, the application of multitemporal images in the same geographical area results in fluctuations in the NDWI threshold. This fluctuation is predominantly attributable to factors such as the geometric configuration of the sun-target-satellite system and prevailing atmospheric conditions.[24]

Notably, contemporary efforts have explored the application of deep learning and machine learning algorithms for detecting watershed areas, showing a progressive shift towards advanced computational techniques in this domain. Studies have recently been conducted on the extraction of water bodies using diverse deep and machine learning technologies.[25–29] Methods such as deep learning enable the rapid and effective extraction of water areas, although substantial quantities of remote sensing training samples are required. Moreover, ongoing studies suggest that object-based image and time-series analyses can be successfully conducted using an algorithm trained using a considerable number of samples.[30] In 2023, a segmentation model called the Segment Anything Model (SAM) was introduced, which was trained using a diverse range of samples.

1.2 Segment Anything Model

SAM was introduced by Meta-AI in April 2023 and was designed to serve as the foundation for a video segmentation model. To achieve this objective, Meta-AI developed a comprehensive large-scale dataset named SA-1B, utilized it to train a model, and subsequently generalized the model. SAM comprises three key components: an image encoder, a versatile prompt encoder, and a rapid mask decoder. SAM was trained using a vast dataset comprising over 1.1 billion masks derived from more than 11 million images, yielding exceptional image segmentation performance.[31]

The robust performance of SAM has prompted extensive research across diverse fields within a short timeframe. Primary investigations focused on applying SAM to medical images, demonstrating its adaptability to healthcare.[30,32,33] Furthermore, SAM has been deployed in the aircraft manufacturing sector to enhance industrial efficiency and has proven to be effective in detecting cracks in civil structures for structural health monitoring purposes.[34,35] The application of SAM extends beyond single-image analysis to video processing.[36] In ongoing studies, the potential of SAM for image segmentation in remote sensing is explored, highlighting its versatile capabilities across various research domains.

Osco *et al.*[(37)] examined the suitability of SAM for remote applications. They found that SAM exhibited commendable performance compared with ground-truth masks, affirming its potential utility in remote sensing applications. However, they used a simplified dataset and emphasized the need to integrate SAM with other methods when dealing with complex datasets. Furthermore, in intricate scenarios, SAM demonstrated suboptimal segmentation results and highlighted the potential variability in accuracy based on the spatial resolution of the input image. Shankar *et al.*[(38)] utilized a SAM algorithm to segment glaciological features, including icebergs, glacier termini, supraglacial lakes, and crevasses. They applied the SAM algorithm to images obtained from diverse sensors, such as Sentinels-1 and 2, planet satellite imagery, and time-lapse photographs, each characterized by varying spatial resolutions. Although the no-prompt approach consistently produced dependable segmentation results across diverse sensors and image types, the results highlighted the necessity of employing the with-prompt method for objects lacking clear features or presenting challenges in differentiating them from the foreground, as exemplified by crevasses. Ren *et al.*[(39)] scrutinized the existing state of marine aquaculture in Liaoning Province, China, using high-resolution satellite imagery. They incorporated the application of the SAM algorithm to analyzing satellite images from GF-1, GF-2, GF-6, and ZY-3. Despite variations in the performance of the SAM algorithm contingent on the aquaculture method, they proposed extending its application to high-resolution remote sensing images in the context of marine aquaculture assessment. In conjunction with optical satellite images, they explored the application of SAM to Synthetic Aperture Radar (SAR) satellite images. Yan *et al.*[(40)] introduced an enhanced RingMo-SAM model that integrates the SAM algorithm into the analysis of SAR images. Consequently, studies have recently been conducted to employ SAM in remote sensing to yield meaningful outcomes. It is imperative to perform a thorough evaluation of the strengths and limitations of the model.

1.3 Research objectives

The aim of this study was to delineate reservoirs using the SAM algorithm and high-resolution satellite images. The algorithm was tested across reservoirs of diverse sizes and shapes under varying weather conditions, reservoirs with different water qualities, and in the presence of structures within the reservoirs. The accuracy of the extracted reservoir was assessed by comparison with visually identified reservoirs, and the precision was evaluated using pixel-based area measurements. This study also involved comparisons with reservoir areas obtained using conventional methods (NDWI images). In addition, we analyzed reservoirs in the Republic of Korea using KOMPSAT-3/3A electro-optical images.

2. Methodology

2.1 Overview

We primarily structured this study into three categories: reservoir extraction by manual image interpretation, reservoir extraction utilizing NDWI images and threshold determination, and reservoir extraction employing the SAM algorithm. In the manual image interpretation, an expert proficient in analyzing remote sensing images visually examined the reservoirs. For the NDWI image segment, NDWI was generated through the conventional method using green and infrared bands, and the reservoirs were identified by determining the optimal threshold among various threshold values. Finally, unsupervised classification was implemented using the SAM algorithm to extract the reservoirs. The pixel-level accuracy of the NDWI-based results and SAM algorithm outcomes were assessed by comparing them with the manual extraction result area, which is considered the standard for true values. Figure 1 shows the flowchart of this study.

2.2 Sensors

KOMPSAT-3 and 3A are South Korean optical satellites developed by the Korea Aerospace Research Institute, featuring an Advanced Electronic Image Scanning System (AEISS). Both satellites deliver high-resolution images, with KOMPSAT-3 housing a panchromatic sensor boasting a ground sample distance (GSD) of 0.7 m and a multispectral sensor with a GSD of 2.8 m. On the other hand, KOMPSAT-3A is equipped with AEISS-A, showcasing enhanced spatial resolution, and operates a panchromatic sensor with a GSD of 0.55 m and a multispectral sensor with a GSD of 2.2 m.[41] Table 1 lists the sensor specifications of KOMPSAT-3/3A.

2.3 Reservoir extraction

2.3.1 Traditional method

Numerous methods and indices have been proposed to extract water bodies, with NDWI, MDNWI, and AWEI being the most commonly used indices. After calculating each index image

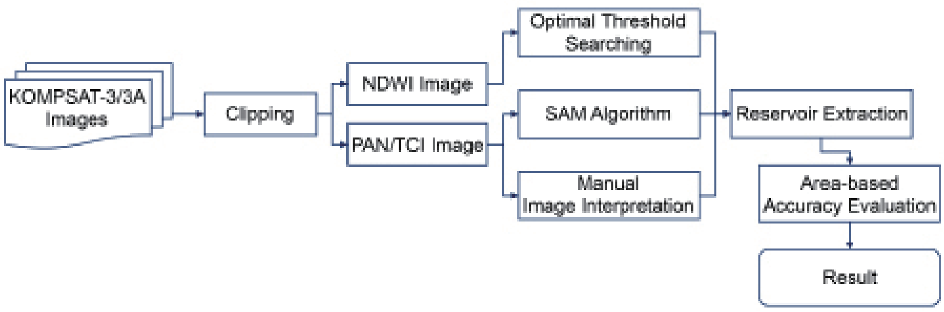

Fig. 1. (Color online) Research flowchart.

Table 1
Specifications of KOMPSAT-3/3A.

		KOMPSAT-3	KOMPSAT-3A
Spectral bands	PAN	450–900 µm	
	MS1 (Blue)	450–520 µm	
	MS2 (Green)	520–600 µm	
	MS3 (Red)	630–690 µm	
	MS4 (NIR)	790–900 µm	
Optics	Focal length	8.6 m	
GSD	PAN	0.7 m at nadir	0.55 m at nadir
	MS	2.8 m at nadir	2.2 m at nadir

based on the satellite-provided bands, determining the water system area involved setting a threshold. In certain instances, an appropriate threshold can be determined manually,(18,42) whereas alternative methods use algorithms to search for the optimal threshold automatically. For this purpose, the Otsu algorithm, introduced in 1979 to select the threshold of a gray-level histogram, is frequently employed.(43) Originally designed for gray-level histograms, it is particularly suitable for binary image classification. The optimal threshold is determined by searching for a value that minimizes the variance within the class. Although studies have utilized the Otsu algorithm for water body determination in the NDWI, MNDWI, and AWEI,(44–46) the findings indicate that this method may not consistently yield optimal results.(17) In this study, we employed a manual thresholding approach to achieve optimal results using NDWI images, facilitating comparison with the outcomes obtained using the SAM algorithm. The NDWI threshold yielding the most suitable results for each image was calculated to enhance the precision of the extraction process.

2.3.2 Geospatial SAM

As mentioned in Introduction, SAM is a specialized algorithm for classifying objects within optical images. Despite the challenges posed by low-spatial-resolution images, SAM demonstrates significant potential and adaptability for analyzing remote sensing data.(37) In contrast, SAM, although extensively trained to distinguish objects, requires adjustments in classification methods to account for terrain characteristics in aerial images.(47) The Geospatial Segment Anything Model (GeoSAM) is a sophisticated algorithm designed to address the challenges of segmenting geospatial features from remote sensing imagery or geospatial data. Unlike traditional segmentation models, GeoSAM is tailored to handle the unique characteristics of geospatial data, including their vast scale, diverse features, and varying resolutions. GeoSAM distinguishes itself from earlier convolutional neural network (CNN)-based methods by achieving superior accuracy in segmenting mobility infrastructure and demonstrating the enhanced capabilities of foundation models in geospatial image analysis.(47) Because of its strength in terrain classification, the GeoSAM algorithm was employed in this study to extract reservoir areas in South Korea.

2.4 Area-based accuracy evaluation

The extracted reservoir area results obtained using NDWI and GeoSAM were compared with the manual extraction results and categorized into three classes. Pixels that aligned with the manual extraction results were termed intersection areas, where higher intersection area values corresponded to increased estimation accuracy. The region covered in the manual extraction results but omitted in the processing outcomes was labeled as the underestimated area. In contrast, the area present in the processing results but absent in the manual extraction results was termed the overestimated area. The accuracy of reservoir extraction diminishes as the underestimated or overestimated area increases. Figure 2 shows the distribution of the intersection, underestimated, and overestimated areas.

The estimation accuracy (P_{acc}), presented as a percentage of the pixel area, can be calculated using Eq. (1).

$$P_{acc} = (A_I - A_U - A_O) / A_R \tag{1}$$

Here, A_I is the intersection area, A_U is the underestimated area, A_O is the overestimated area, and A_R is the area of the reservoir.

3. Case Study

3.1 Study area

We conducted experiments on reservoirs of diverse sizes and shapes distributed across the Republic of Korea. KOMPSAT-3/3A images capturing each reservoir were carefully chosen, and the region of interest (ROI) was extracted. In the experiment, we used a set of 10 satellite images

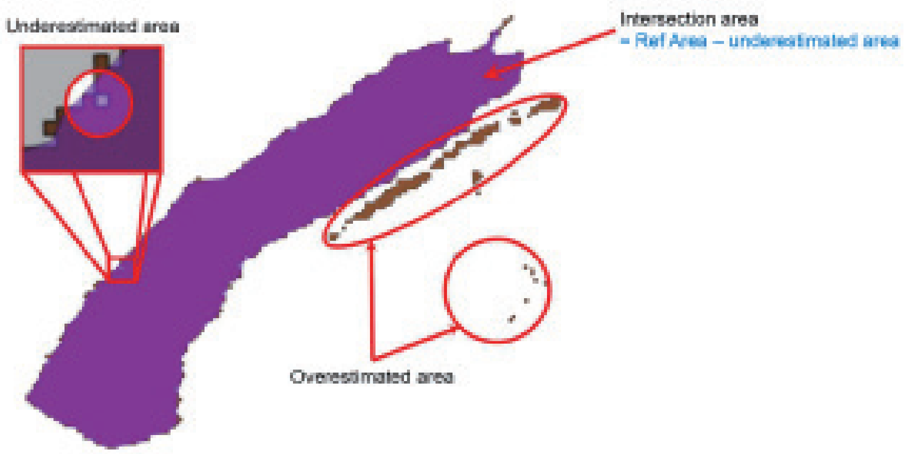

Fig. 2. (Color online) Classification of reservoir extraction results: intersection area, underestimated area, and overestimated area.

comprising seven different reservoirs. Emphasis was placed on using images from clear days when the reservoir was distinctly visible. Images featuring cloud cover, occurrence of red-green algae in the reservoir, or instances of reservoir freezing were excluded from the accuracy evaluation. Figure 3 visually represents the distribution and shapes of the targeted reservoirs, whereas Table 2 lists the latitude and longitude coordinates of the center point of the satellite image, satellite type, and imaging dates.

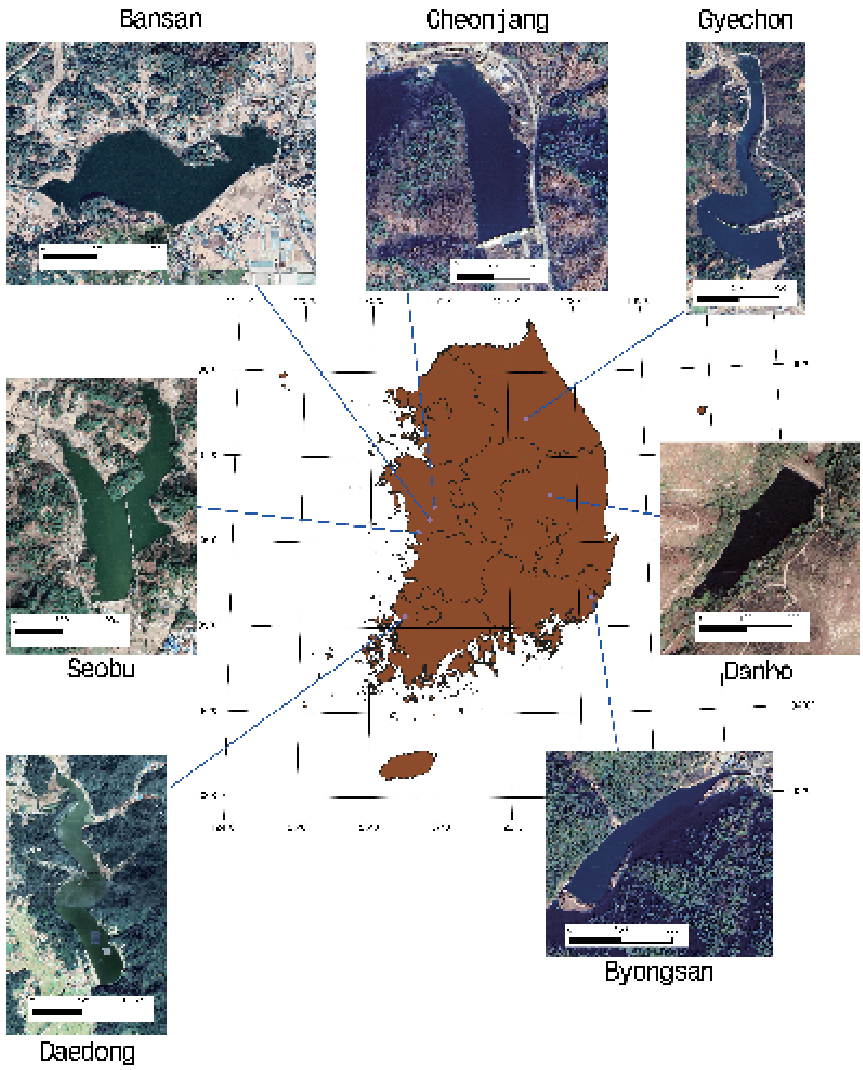

Fig. 3. (Color online) Shapes and distribution of reservoirs.

Table 2
Details of reservoirs and satellite images.

Province	Name	Latitude	Longitude	Satellite	Date
Busan	Byongsan	35.3444	129.1822	K3	20141109
				K3A	20220329
Chungcheongnam-do	Bansan	36.2731	126.8469	K3	20150425
				K3	20171106
	Seobu	36.1272	126.6911	K3	20140316
	Cheonjang	36.4150	126.9181	K3	20141202
Gangwon-do	Gyechon	37.4575	128.2808	K3	20190524
Gyeongsangbuk-do	Danho	36.5533	128.6106	K3	20150207
Jeollanam-do	Daedong	35.1322	126.5064	K3	20150320
				K3A	20170908

3.2 Results

3.2.1 Traditional method vs GeoSAM

In this subsection, we present a comparative analysis of the GeoSAM results and the results of the traditional method of water body extraction using NDWI. To facilitate this, an NDWI image was generated using the green and NIR bands of each satellite image, followed by the creation of a binary image by adjusting the threshold in increments of 0.05. The threshold with the highest accuracy for reservoir extraction was systematically identified for each image. Table 3 presents the accuracy of water body extraction for each threshold.

The optimal threshold value was determined individually for each image because of the variations in imaging areas and times. Except for Cheonjang-K3-20190524 and Daedong-K3A-20170908, the optimal threshold values were generally between 0.15 and 0.25. Figure 4 shows an illustrative example of determining the aqueous and nonaqueous areas by adjusting the threshold for the Gyechon-K3-20141202 image.

The optimal threshold for each image captured with the ROIs was determined, and the estimated results were compared with those obtained using GeoSAM. Table 4 presents a comparison of the results obtained by the GeoSAM- and NDWI-based methods for each region and image.

GeoSAM exhibited outstanding estimation results in certain cases, whereas NDWI demonstrated excellent estimation results. On average, the estimation results were slightly superior when GeoSAM was used. GeoSAM consistently exhibited excellent performance in cases where NDWI yielded exceptional outcomes. However, in cases where GeoSAM performed exceptionally well, there were situations in which the NDWI-based method exhibited relatively lower accuracy (Bansan-K3-20171106, Gyechon-K3-20141202, and Daedong-K3A-20170908).

Figure 5 shows the RGB representations of the satellite images corresponding to each reservoir, the region delineated using NDWI (indicated by the yellow shapefile), and the reservoir area delineated using GeoSAM (represented by the blue shapefile). Notably, the outcomes derived from the NDWI revealed that areas beyond the reservoir boundaries were also identified as water systems. In contrast, the GeoSAM-extracted results demonstrated a

Table 3
Evaluation of reservoir extraction accuracy according to threshold.

Name	Accuracy based on NDWI threshold (%)								
	−0.1	−0.05	0	0.05	0.1	0.15	0.2	0.25	0.3
Byongsan							57.88	**85.08**	27.66
					96.01	**96.78**	89.68	1.05	
Bansan					95.37	96.50	**96.80**	96.50	86.56
					86.05	86.16	**88.98**	87.61	84.06
Seobu					89.20	**94.16**	93.59	0.10	
Cheonjang					−41.21	22.93	**90.99**	23.42	
Gyechon	93.62	**94.81**	73.00						
Danho					89.71	95.08	**97.38**	95.83	80.96
Daedong					94.19	95.08	**96.00**	31.02	
			85.33	**86.22**	82.31	73.65	51.78		

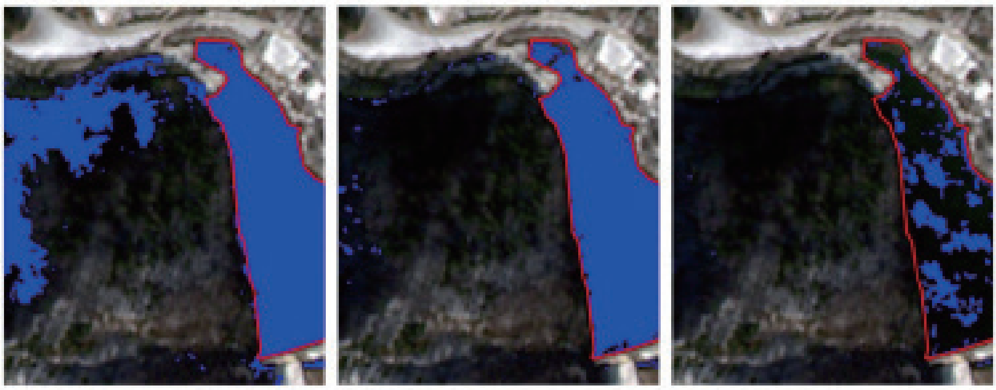

(a) (b) (c)

Fig. 4. (Color online) Binary images of the Gyechon case (blue, extracted area; red line, manually extracted area; background image, KOMPSAT-3 imagery). (a) Threshold = 0.15, (b) Threshold = 0.20 (highest accuracy), and (c) Threshold = 0.20.

Table 4
Comparison of accuracy between GeoSAM- and NDWI-based methods.

Name	Satellite Date	Accuracy (%)	
		GeoSAM	NDWI (optimal threshold)
Byongsan	K3-20141109	**85.95**	85.08
	K3A-20220329	**97.10**	96.78
Bansan	K3-20150425	96.04	**96.80**
	K3-20171106	**93.97**	88.98
Seobu	K3-20140316	92.66	**94.16**
Cheonjang	K3-20141202	**94.57**	90.99
Gyechon	K3-20190524	**95.73**	94.28
Danho	K3-20150207	94.02	**97.38**
Daedong	K3-20150320	95.13	**96.00**
	K3A-20170908	**92.23**	86.22
Average Accuracy		**93.74**	92.67

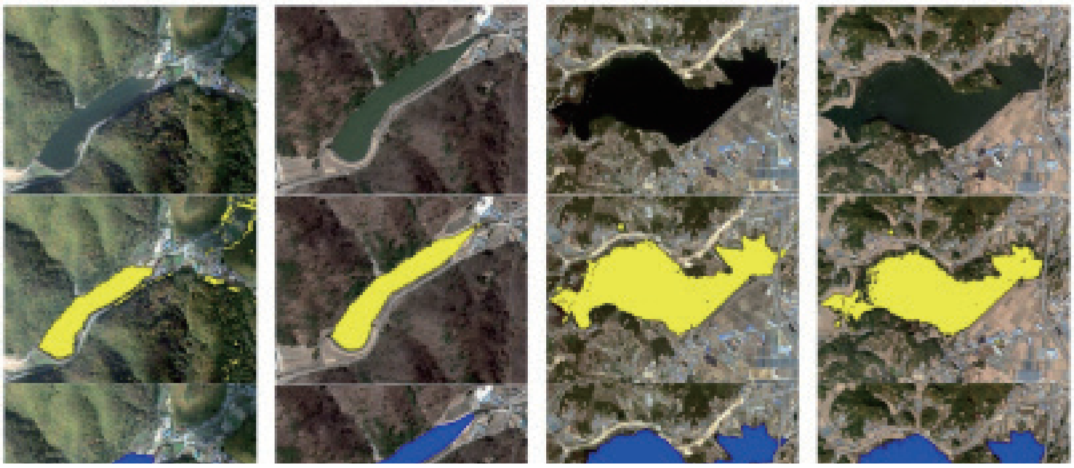

(a) (b) (c) (d)

Fig. 5. (Color online) Images of Byongsan: RGB image (top), NDWI-based extracted region (middle), and GeoSAM-based extracted region (bottom). (a) Byongsan-K3, (b) Byongsan-K3A, (c) Bansan-K3, and (d) Bansan-K3.

discernible absence of noncontiguous areas, with only a few regions extracted outside the reservoir boundaries.

3.2.2 Extraction results under challenging conditions

In this study, GeoSAM algorithm extraction results were tested using high-resolution satellite images with ambiguous reservoir visibility. Special scenarios captured in the satellite images included cases when the reservoir bottom was exposed during dry periods, shadows were cast on the water surface, part or all of the water surface was frozen, a bridge spanned across the reservoir, clouds obstructed the reservoir, artificial structures were present on the water surface, and red-green algae were present in the reservoir.

Figure 6 shows a scenario in which the bottom of the reservoir was exposed during the dry season. In images showing dry-water conditions, where the water volume decreased and a portion of the bottom was revealed, isolated water puddles were possibly present [Fig. 6(a)]. Without the addition of the mask points, these isolated puddles were excluded from the extraction [Fig. 6(b)]. However, if mask points were added to comprise these areas, regions where water did not exist were included [Fig. 6(c)]. The bottom part was eliminated by manually introducing a negative mask point [Fig. 6(d)].

When dealing with images in which shadows conceal the water surface, dark-shadowed areas are not automatically recognized as water areas by the GeoSAM algorithm. Consequently, placing additional mask points strategically is necessary. However, introducing these additional points can result in false positives, requiring the use of negative mask points to correct the extraction and eliminate inaccuracies (Fig. 7).

In cases where part of the water surface was frozen, the entire reservoir could sometimes be accurately delineated using a single mask point [Fig. 8(a)]. However, extracting the complete reservoir area using GeoSAM proved challenging in most cases, particularly when the water

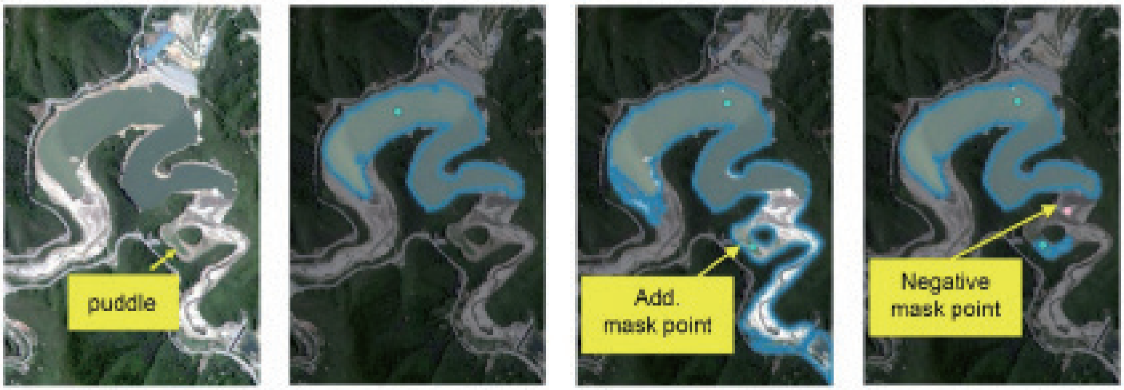

(a) (b) (c) (d)

Fig. 6. (Color online) Results of applying the GeoSAM algorithm to the dry season image: (a) reservoir in the dry season, (b) initial result, (c) adding mask point, and (d) adding negative mask point.

(a) (b) (c)

Fig. 7. (Color online) Results of applying the GeoSAM algorithm to the shadowed image: (a) shadowed image, (b) false negatives caused by shadows, and (c) additional mask point and negative mask point placement.

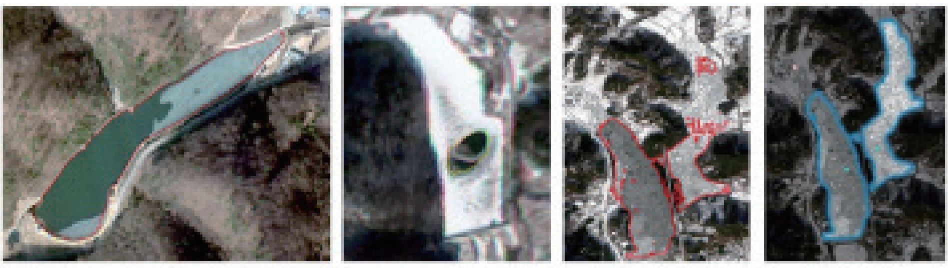

(a) (b) (c) (d)

Fig. 8. (Color online) Results of applying the GeoSAM algorithm to the frozen reservoir. (a) Fully extracted case, (b) partially extracted case, (c) fully frozen case, and (d) adding mask points and negative mask points.

surface was partially or fully frozen [Figs. 8(b) and 8(c)]. When the reservoir was entirely frozen and was difficult to distinguish from the surrounding environment, extracting the entire reservoir area using GeoSAM was particularly difficult [Fig. 8(c)]; this required using multiple negative mask points to refine the extraction process [Fig. 8(d)]. However, distinguishing between reservoirs was challenging under completely frozen conditions, even with visual inspection.

The GeoSAM algorithm did not consistently extract the entire reservoir area when there was a fluctuation in the reservoir water surface, such as a red-green tide. Areas affected by red or green tides were frequently misclassified as land or vegetation [Figs. 9(a) and 9(b)].

4. Discussion

4.1 Traditional methods vs GeoSAM

We conducted a comparative analysis between the traditional NDWI-based and GeoSAM-based extraction methods using KOMPSAT-3/3A satellite images. The exploration involved determining the optimal NDWI threshold within the range from 0.15 to 0.25, successfully detecting over 89.24% of the reservoir area near this threshold range. However, importantly, the optimal threshold did not consistently fall within this range for all cases. In certain instances, a very low threshold, such as 0.05 or less, was deemed optimal. This variability can be attributed to diverse topographical, climatic, and seasonal factors.[21] The literature indicated that the distribution of surrounding trees, chemical/biological substances in water, and water vapor distribution may influence NDWI thresholds. Shadows on typical terrains (such as bushes and mountains) can elevate the NDWIs, resembling those of water body areas. Additionally, low NDWIs were identified in areas affected by red or green tides and in regions obscured by clouds. The selection of the NDWI threshold is critical for accurate water surface area estimation; however, fixed thresholds may result in low reservoir estimation accuracy because of the potential for false detections arising from various factors.

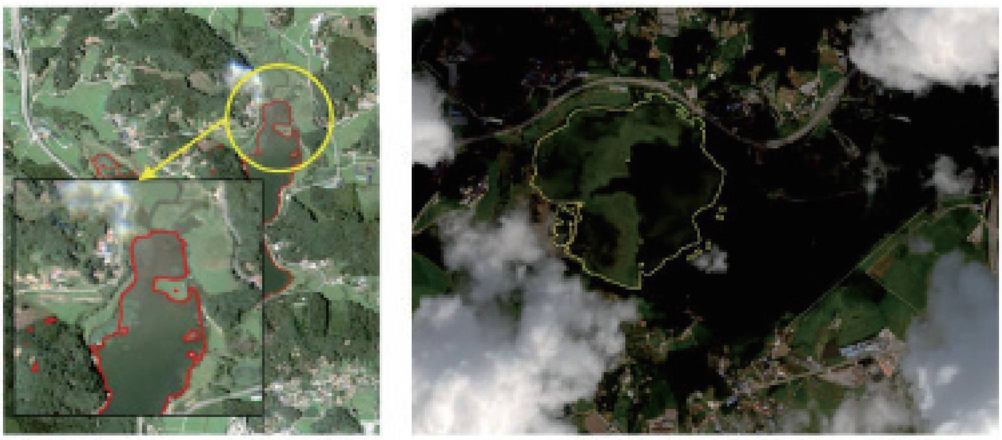

(a) (b)

Fig. 9. (Color online) Results of applying GeoSAM to a reservoir with the tide: (a) small-scale red-green algae and (b) a harsh image case with poor image quality and red-green tide.

In the GeoSAM-based method, the accuracy of the estimations, both at the lowest and highest ends, was marginally superior to that of the existing NDWI-based method. GeoSAM minimized the noncontinuous regions within the largest water surface area (areas that appeared as noise in the NDWI results). This deviation arises because GeoSAM does not rely on pixel-by-pixel threshold classification, as in the NDWI-based method, but instead categorizes classes on the basis of their contiguity with the largest mask. Figures 5–7 show that the GeoSAM-based method yielded results more similar to those perceived by the human eye. However, in situations where the distinction between aqueous and nonaqueous systems is ambiguous, such as at the boundary of a reservoir, the model may produce inaccurate assessments.

In addition to its enhanced accuracy and robustness, GeoSAM entails a higher computational cost than the NDWI-based method. Specifically, GeoSAM employs advanced deep learning techniques that necessitate graphics processing unit (GPU) acceleration and involve iterative prompt-based refinements, leading to processing times of approximately 5–10 min per high-resolution image. In contrast, the NDWI-based approach, which relies on straightforward spectral thresholding, processes images in about 1–2 min on a CPU, albeit with lower performance under challenging conditions. As summarized in the table below, this comparison highlights the trade-offs between superior extraction accuracy and increased resource demands. This information should prove valuable for practitioners assessing the resource feasibility of implementing GeoSAM for reservoir monitoring.

4.2 Extraction results in challenging environments

In this study, we applied GeoSAM to satellite images captured in challenging environments through additional experiments. Experiments were conducted for various scenarios, including freezing, exposed reservoir bottoms during dry periods, fog and clouds, shadows, the presence of structures, and the occurrence of red-green tides. The results revealed a significant decrease in reservoir extraction accuracy compared with the initial outcomes. In particular, in cases with thick clouds or when the reservoir was completely frozen, proper reservoir extraction did not occur. Considering that even human visual interpretation is challenging in such environmental images, it is reasonable for the extraction to be unsuccessful. Although utilizing imaging sensors operating at different wavelengths, such as SAR images, could potentially distinguish these environments, this was beyond the scope of this study.

Similarly to GeoSAM, the NDWI-based method also encountered difficulty in accurately extracting watershed areas. Each anomaly altered the NDWI value, leading to a distinct separation between the watershed area and the anomaly-affected region. In contrast, GeoSAM facilitates the restoration of unextracted reservoirs through additional point prompts. The addition of mask points during the dry season, when shadows covered the reservoir or when parts of the water surface were frozen, increased the reservoir area. However, the addition of mask points resulted in false negatives, which could be rectified by adding negative mask points. Although GeoSAM demonstrates excellent performance with ideal satellite images, it is evident that human intervention continues to be vital in suboptimal imaging environments.

In fully frozen reservoirs, GeoSAM's performance was compromised by several interrelated factors. First, the spectral similarity between ice and water significantly reduces the contrast needed for effective segmentation, posing challenges for deep learning algorithms that rely on distinct spectral features to delineate reservoir boundaries. Additionally, the reflective properties of frozen surfaces often lead to irregular shadow patterns, introducing noise into the remote sensing imagery and complicating the extraction process, which may result in misclassifications during reservoir monitoring. Finally, the sensitivity to the initial point or box prompts becomes more pronounced under these conditions; the limited variability in pixel intensity and texture in frozen environments diminishes the effectiveness of these spatial cues, making it more difficult for GeoSAM to accurately distinguish the reservoir from its surroundings.

5. Conclusions

In this study, we compared the traditional NDWI-based water extraction method with the GeoSAM-based method using KOMPSAT-3/3A satellite images and conducted experiments on reservoirs of diverse sizes and shapes on the Korean Peninsula. The accuracy of the extracted areas was assessed by a remote sensing expert who created reference data through visual inspection.

For the NDWI-based method, optimal accuracy occurred with a threshold between 0.15 and 0.25, yielding an accuracy range of 85.08–97.38%, with an average of 92.67%. The GeoSAM-based method achieved an accuracy range of 85.95–97.10%, with an average of 93.74%. GeoSAM consistently demonstrated high accuracy and was visually aligned with the human-accepted results.

We also examined the estimation results under various scenarios, including frozen reservoirs, shadowed areas, cloudy conditions, artificial structures, and red-green algae. The estimation accuracy could be compromised in these situations, a trend that was also observed for the NDWI-based method. The accuracy of GeoSAM can be enhanced by introducing additional points or box prompts.

Acknowledgments

This work was supported by the Basic Science Research Program through the National Research Foundation of Korea (NRF), funded by the Ministry of Science, ICT (MSIT) (grant number 2022R1G1A1005391) and 'Satellite Information Application' of the Korea Aerospace Research Institute (KARI).

References

1 X. Cai, L. Feng, X. Hou, and X. Chen: Sci. Rep. **6** (2016) 36405. https://doi.org/10.1038/srep36405
2 H. Gao, C. Birkett, and D. P. Lettenmaier: Water Resour. Res. **48** (2012). https://doi.org/10.1029/2012WR012063
3 H. Gao: WIREs Water. **2** (2015) 147. https://doi.org/10.1002/wat2.1065
4 V. S. Martins, A. Kaleita, C. C. F. Barbosa, A. C. Fassoni-Andrade, F. L. Lobo, and E. M. L. M. Novo: Remote Sens. Appl.: Soc. Environ. **13** (2019) 275. https://doi.org/10.1016/j.rsase.2018.11.006
5 T. Chen, C. Song, P. Zhan, J. Yao, Y. Li, Y., and J. Zhu: Sci. Total Environ. **807** (2022) 150772. https://doi.org/10.1016/j.scitotenv.2021.150772

6 Y. Du, Y. Zhang, F. Ling, Q. Wang, W. Li, and X. Li: Remote Sens. **8** (2016) 354. https://doi.org/10.3390/rs8040354
7 X. Yang, Q. Qin, H. Yésou, T. Ledauphin, M. Koehl, P. Grussenmeyer, and Z. Zhu: Remote Sens. Environ. **244** (2020) 111803. https://doi.org/10.1016/j.rse.2020.111803
8 N. Avisse, A. Tilmant, M. F. Müller, and H. Zhang: Hydrol. Earth Syst. Sci. **21** (2017) 6445. https://doi.org/10.5194/hess-21-6445-2017
9 Z. Du, B. Linghu, F. Ling, W. Li, W. Tian, H. Wang, Y. Gui, B. Sun, and X. Zhang: J. Appl. Remote Sens. **6** (2012) 63609. https://doi.org/10.1117/1.JRS.6.063609
10 B. C. Naik and B. Anuradha: Int. J. Electr. Comput. Eng. **8** (2018) 4111. https://doi.org/10.11591/ijece.v8i6.pp4111-4119
11 M. G. Tulbure and M. Broich: ISPRS J. Photogramm. Remote Sens. **79** (2013) 44. https://doi.org/10.1016/j.isprsjprs.2013.01.010
12 T. Guan, Q. Xu, X. Chen, and J. Cai: Hydrol. Res. **52** (2021) 1066. https://doi.org/10.2166/nh.2021.035
13 S. J. Park and C. W. Lee: Korean J. Remote Sen. **34** (2018) 1319. https://doi.org/10.7780/kjrs.2018.34.6.3.2
14 H. J. You and H. Choi: J. Korean Soc. Ind. Converg. **23** (2020) 173. https://doi.org/10.21289/KSIC.2020.23.2.173
15 B. C. Gao: Remote Sens. Environ. **58** (1996) 257. https://doi.org/10.1016/S0034-4257(96)00067-3
16 H. Xu: Int. J. Remote Sens. **27** (2006) 3025. https://doi.org/10.1080/01431160600589179
17 Q. Guo, R. Pu, J. Li, and J. Cheng: Int. J. Remote Sens. **38** (2017) 5430. https://doi.org/10.1080/01431161.2017.1341667
18 K. Rokni, A. Ahmad, A. Selamat, and S. Hazini: Remote Sens. **6** (2014) 4173. https://doi.org/10.3390/rs6054173
19 F. Pan, X. Xi, and C. Wang: Remote Sens. **12** (2020) 1611. https://doi.org/10.3390/rs12101611
20 Z. Du, W. Li, D. Zhou, L. Tian, F. Ling, H. Wang, Y. Gui, and B. Sun: Remote Sens. Lett. **5** (2014) 672. https://doi.org/10.1080/2150704X.2014.960606
21 L. Ji, L. Zhang, and B. Wylie: Photogramm. Eng. Remote Sens. **75** (2009) 1307. https://doi.org/10.14358/PERS.75.11.1307
22 F. Chen, X. Chen, T. Van de Voorde, D. Roberts, H. Jiang, and W. Xu: Remote Sens. Environ. **242** (2020) 111706. https://doi.org/10.1016/j.rse.2020.111706
23 X. Yang, S. Zhao, X. Qin, N. Zhao, and L. Liang: Remote Sens. **9** (2017). 596. https://doi.org/10.3390/rs9060596
24 Y. Liu: 2012 IEEE Int. Geoscience and Remote Sensing Symposium (IEEE, Munich, Germany, 2012). 4375–4378. https://doi.org/10.1109/IGARSS.2012.6350404
25 Y. Chen, R. Fan, X. Yang, J. Wang, and A. Latif: Water **10** (2018) 585. https://doi.org/10.3390/w10050585
26 X. Huang, C. Xie, X. Fang, and L. Zhang: IEEE J. Sel. Top. Appl. Earth Obs. Remote Sens. **8** (2015) 2097. https://doi.org/10.1109/JSTARS.2015.2420713
27 M. Li, P. Wu, B. Wang, H. Park, Y. Hui, and W. Yanlan: IEEE J. Sel. Top. Appl. Earth Obs. Remote Sens, **14** (2021) 3120. https://doi.org/10.1109/JSTARS.2021.3060769
28 Z. Wang, X. Gao, Y. Zhang, and G. Zhao: Remote Sens. **12** (2020) 4140. https://doi.org/10.3390/rs12244140
29 S. Zhu and J. Mao: Remote Sens. **13** (2021) 249. https://doi.org/10.3390/rs13132498
30 J. Ma, Y. He, F. Li, L. Han, C. You, and B. Wang: Nat. Commun. **15** (2024) 654. https://doi.org/10.1038/s41467-024-44824-z
31 A. Kirillov, E. Mintun, N. Ravi, H. Mao, C. Rolland, L. Gustafson, T. Xiao, S. Whitehead, A. C. Berg, W. Y. Lo, P. Dollar, and R. Girshick: Proc. IEEE/CVF Int. Conf. Computer Vision (IEEE, Paris, France, 2023), 4015–4026. https://doi.org/10.48550/arXiv.2304.02643
32 Y. Huang, X. Yang, L. Liu, H. Zhou, A. Chang, and X. Zhou: Med. Image Anal. **92** (2024) 103061. https://doi.org/10.1016/j.media.2023.103061
33 M. A. Mazurowski, H. Dong, H. Gu, J. Yang, N. Konz, and Y. Zhang: Med. Image Anal. **89** (2023) 102918. https://doi.org/10.1016/j.media.2023.102918
34 K. Moenck, A. Wendt, P. Prünte, J. Koch, A. Sahrhage, J. Gierecker, O. Schmedemann, F. Kähler, D. Holst, M. Gomse, T. Schüppstuhl, and D. Schoepflin: arXiv Prepr (2023) arXiv2307.12674.
35 M. Ahmadi, A. G. Lonbar, A. Sharifi, A. T. Beris, M. Nouri, and A. S. Javidi: arXiv Prepr (2023) arXiv2304.12600.
36 J. Yang, M. Gao, Z. Li, S. Gao, F. Wang, and F. Zheng: arXiv Prepr (2023) arXiv2304.11968.
37 L. P. Osco, Q. Wu, E. L. de Lemos, W. N. Gonçalves, A. P. M. Ramos, J. Li, J., and J. M. Marcato: Int. J. Appl. Earth Obs. Geoinf. **124** (2023) 103540. https://doi.org/10.1016/j.jag.2023.103540.
38 S. Shankar, L. A. Stearns, and C. J. van der Veen: J. Glaciol. **70** (2023) 1. https://doi.org/10.1017/jog.2023.95.
39 Y. Ren, X. Yang, Z. Wang, G. Yu, Y. Liu, X. Liu, D. Meng, Q. Zhang, and G. Yu: Remote Sens. **15** (2023) 5781. https://doi.org/10.3390/rs15245781.
40 Z. Yan, J. Li, X. Li, R. Zhou, W. Zhang, Y. Feng, W. Diao, K. Fu, and X. Sun: IEEE Trans. Geosci. Remote Sens. **61** (2023) 1. https://doi.org/10.1109/TGRS.2023.3332219.

41 N. Kim, Y. Choi, J. Bae, and H. G. Sohn: GISci. Remote Sens. **57** (2020) 719. https://doi.org/10.1080/15481603.2020.1791499
42 E. Özelkan: Pol. J. Environ. Stud. **29** (2020) 1759. https://doi.org/10.15244/pjoes/110447.
43 N. Ostu: SMC IEEE (Trans) **9** (1979) 62.
44 T. D. Acharya, D. H. Lee, A. Subedi, and H. Huang, H: Sens. Mater. **31** (2019) 10. https://doi.org/10.18494/SAM.2019.2264.
45 W. Li, Z. Du, F. Ling, D. Zhou, H. Wang, Y. Gui, B. Sun, and X. Zhang: Remote Sens. **5** (2013) 5530. https://doi.org/10.3390/rs5115530.
46 H. Yue, Y. Li, J. Qian, and Y. Liu: Int. J. Remote Sens. **41** (2020) 7311. https://doi.org/10.1080/01431161.2020.1755740.
47 R. I. Sultan, C. Li, H. Zhu, P. Khanduri, M. Brocanelli, and D. Zhu: arXiv Prepr (2023) arXiv2311.11319.